



Physical characterization of 5',5''-dibromo-o-cresolsulfophthalein (BCP) spin-coated thin films and BCP/p-Si based diode

A. M. Mansour^{1,2} · Mahmoud Nasr¹ · H. A. Saleh³ · G. M. Mahmoud¹

Received: 29 May 2019 / Accepted: 8 August 2019 / Published online: 16 August 2019
© Springer-Verlag GmbH Germany, part of Springer Nature 2019

Abstract

The organic 5',5''-dibromo-o-cresolsulfophthalein (BCP) compound thin films were deposited simply through spin coating technique from a pre-prepared solution of different molarities. Differential thermal analysis (DSC) and thermogravimetric analysis (TGA) of the starting powder compound were investigated to obtain the thermal stability and phase transformation of the compound. The structure, morphology, and optical properties were analyzed for all the prepared films of different molarities. Structural analyses revealed the nanocrystalline composition of all the prepared thin films. The resulted thin films nanostructure feature is verified by utilizing both the field emission scanning-electron-microscope (FESEM) and the high-resolution transmission electron microscope (HRTEM). Optical absorption exploration of BCP thin films was carried out in the limit of 200–2500 nm wavelength. The results revealed no changes in optical properties with molarity change. Al/p-Si/BCP/Au junction was prepared and investigated electrically in dark conditions and the diode parameters were extracted. The obtained diode can be employed in many applications such as rectifiers, clipper circuits, clamping circuits, reverse current protection circuits, logic gates, voltage multipliers, flexible electronics, and many other optoelectronic applications.

Keywords Bromocresolpurple · Structure · DSC-TGA · Current–Voltage · Diode

1 Introduction

Organic semiconductors are generally π -conjugated networks. They are divided into a couple of categories according to the molecular weight [1]: high molecular weight conjugated polymers and low molecular weight molecules. Each of those groups shares a conjugated p-electron created by the p_z orbitals of sp^2 hybridized C atoms in the molecules [2]. The electronic benefits of a molecule depend upon the length of the conjugation bond or the existence of electron giving groups. π -electrons are generally delocalized and can revolve in the region of the molecular plane. Even so, the molecular

chain turn into larger, the π -electrons amount increases and an enhance in electrical conductivity is attained [3–5]. π bonding is critically weaker than in σ bonds presented in the molecule backbone. Subsequently, the minimum electronic excitations of conjugated molecules are the π – π^* transitions [6]. The energy gap in most cases is from 1.5 to 3 eV resulting in visible spectral absorption or emission [7]. It may be possible to outline the variables that develop a good organic semiconducting device as [8, 9]: the existence of a conjugated structure, the π -electronic cloud could be overlapped, good thin film structural benefits, chemical purity, and material stability. Hence organic chemistry supplies a wide variety of opportunities to tune the optoelectronic benefits of organic semiconductors. Organic substances practically have an unlimited number and unlimited size extent from simple molecules to polymers [10]. These characteristics considerably raise the limit of selection and designing opportunities and applications of organic semiconductors such as photo-sensors, photovoltaic devices, transistors, and light-emitting diodes [11].

Bromocresol purple (BCP) dye, 5',5''-dibromo-o-cresol-sulfophthalein, is a sulfonephthalein dye wherein the phenyl group is linked to the main carbon atom, Fig. 1a. BCP dye

✉ A. M. Mansour
amamansour@gmail.com

¹ Solid-State Electronics Laboratory, Physics Research Division, Solid-State Physics Department, National Research Centre, 33 El-Bohouth St., Dokki, Giza 12622, Egypt

² Center of Microelectronics in Provence, Mines Saint-Etienne, 13541 Gardanne, France

³ Electron Microscope and Thin Films Department, Physical Research Division, National Research Centre, 33 El-Bohouth St., Dokki, Giza 12622, Egypt

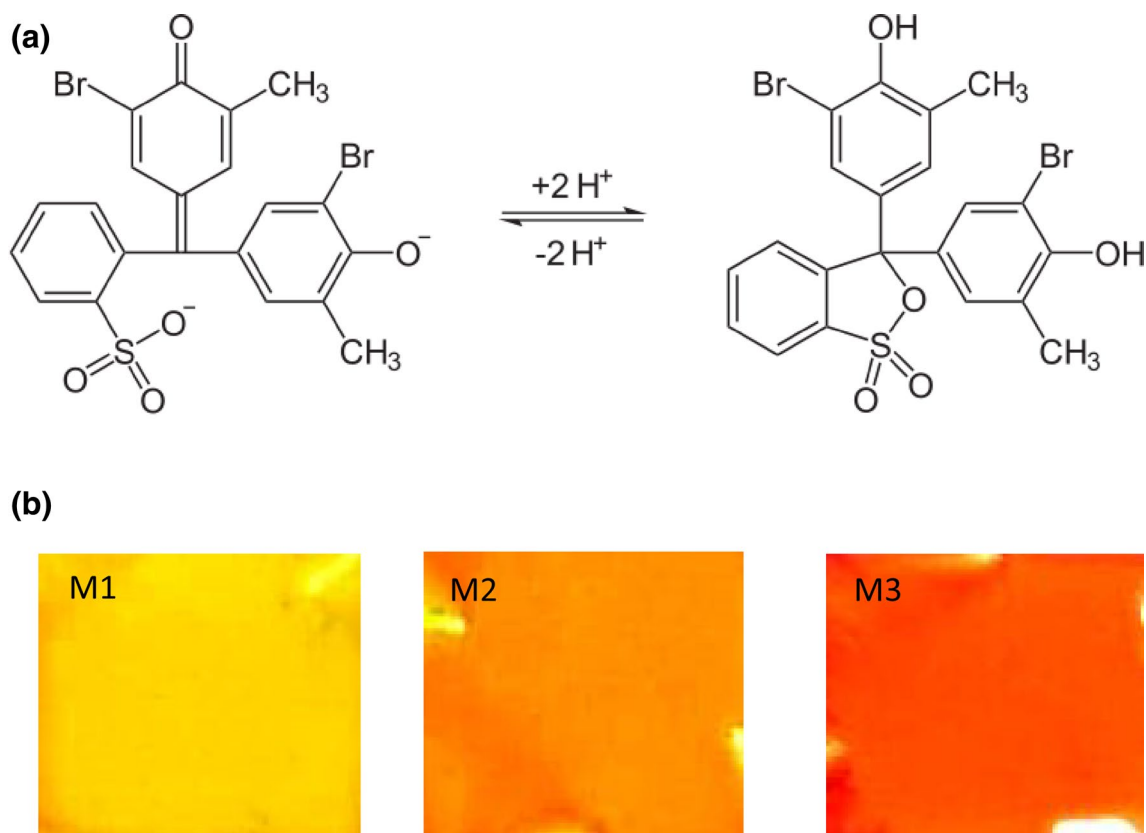


Fig. 1 **a** The BCP molecule rehybridization from unsymmetrical resonance scheme to symmetric one and vice versa which is responsible for coloring transformation, and **b** The resultant deposited films of different molarities on glass substrates

is usually utilized as pH references. It provides a yellow-colored in alkaline conditions and gets a red-hue at acidic conditions [12]. BCP provides superior conductivity due to its π - π conjugated bonds, considerable surface area and an elevated amount of active side [13]. The BCP coloring transformation is resulted from molecule rehybridization from unsymmetrical resonance scheme to symmetric one and vice versa and also from surrounding environment polarity changing [12, 14], as in Fig. 1a. Consequently, the BCP dye exhibits its characteristic absorption in a nonpolar solvent [15]. The 2nd order hyperpolarizabilities of BCP dye molecule loses when the solvent polarity or dielectric constant decreases [12]. BCP was utilized in detecting albumin, hypoxanthine, uric acid and xanthine [16]. Over a wide variety of heat and humidness, BCP doped polymer film was used as an ammonia gas detector [17]. L-Tyrosine detecting sensor was developed using a BCP improved carbon electrode [18]. An organic photodiode based on BCP was prepared by conventional thermal evaporation [19]. A 1.9 eV optical band gap was observed [19].

In the current study, 5',5''-dibromo-o-cresolsulphthalein (BCP) thin films were spin-coated from different molarities solutions. The effect of molarity change on structural, morphological, and optical features of the resulted thin films was

inspected. BCP stableness against thermal decomposition and phase transformation were checked out with DSC and TGA techniques. Additionally, a device junction of Al/p-Si/BCP/Au was manufactured and its dark electrical properties were inspected.

2 Materials, samples preparation, and experimental methods

The powder of BCP used in this study was produced by Sigma Aldrich and it was employed as supplied without extra processing. Spin coating technique was used to deposit BCP thin films on glass and Si substrates at 2400 rpm and at room temperature for all the deposited films. In the preparation of BCP films, a solution with different molarities ($M1 = 1M$, $M2 = 2M$, and $M3 = 3M$) of BCP was dissolved in ethanol using magnetic stirrer for 30 minutes. The resultant solution was deposited on glass substrates as presented in Fig. 1b. The solution of molarity 3M was chosen to be deposited on Si substrates for a device preparation and examining trial purpose. Every BCP molarity is spin coated with a single layer for 2 min and then the thickness of the layer has been increased by successive spin coating of 3-layers.

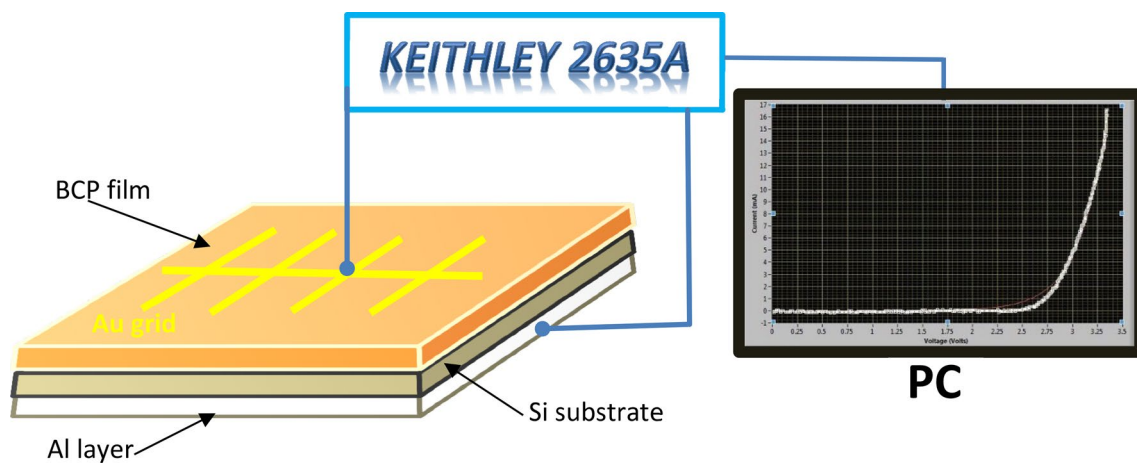


Fig. 2 Schematic diagram of the device layers and circuit arrangement of I - V measurements

The thickness of the films was measured by the conventional gravimetric method and it was found in the range of $400 \text{ nm} \pm 10\%$. Finally, the films are kept to dry at room temperature. A glass and p-Si substrates employed in fabricating thin films and the heterojunctions were chemically washed by the method outlined elsewhere [20, 21]. Aluminum ohmic contact and a gold electrode (about 100 nm layer) were deposited on the back surface of Si and BCP film in front of the prepared junction, respectively. The metal electrodes were deposited by means of a thermal coating machine Edwards E 306 A at room temperature, the vacuum of about 1.33×10^{-6} kPa before the evaporation process starting, and 2 nm/s deposition rate. A schematic diagram of the prepared device layers can be seen in Fig. 2.

Philips X'pert goniometer employing copper target (CuK_α) powered at 40 kV and 25 mA was employed in studying the structure of the prepared films while the morphology of the films was observed and visualize with two means, the SEM (Quanta FEG 250) and Joel JEM 2100 high-resolution transmission electron microscope.

In a nitrogen environment and heating rate of $10^\circ\text{C}/\text{min}$, differential scanning calorimetry (DSC) and thermogravimetric analysis (TGA) of starting BCP powder were done by SDTQ 600 thermogravimetric analyzer unit.

BCP films optical and bandgap benefits in the wavelength range of 200–2500 nm were examined by employing UV-VIS-NIR spectrophotometer JASCO, V-570.

The manufactured device, i.e. Al/p-Si/BCP/Au heterojunction, dark current-voltage properties were explored at different temperature by means of KEITHLEY 2635A source-meter as shown in Fig. 2.

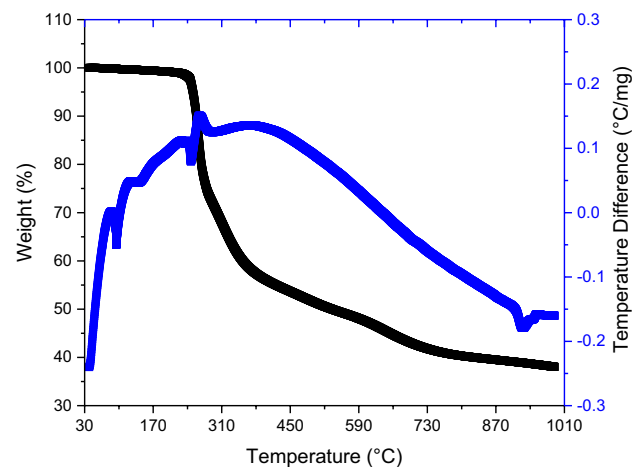


Fig. 3 DSC and TGA thermogram of BCP starting powder

3 Results and discussions

3.1 Phase transition and thermal stability

In nitrogen (N_2) atmosphere, thermal analysis by both DSC and TGA of BCP were achieved at $10^\circ\text{C}/\text{min}$ heating rate and the results are presented in Fig. 3. The output thermogram of DSC displays three events of the endothermic type in the heating range developed at 96°C , 146°C , 247°C , and 925°C respectively. The endothermic peak occurred at a 96°C is referred to the glass transition or the transition from glassy to rubber-like state process that induced as a result of motion unfreezing of simple kinetics including Br, CH_3 , and OH [22]. The endothermic event at 146°C may relate to rehybridization from unsymmetrical to symmetric resonance [14]. At 247°C , the decomposition event is

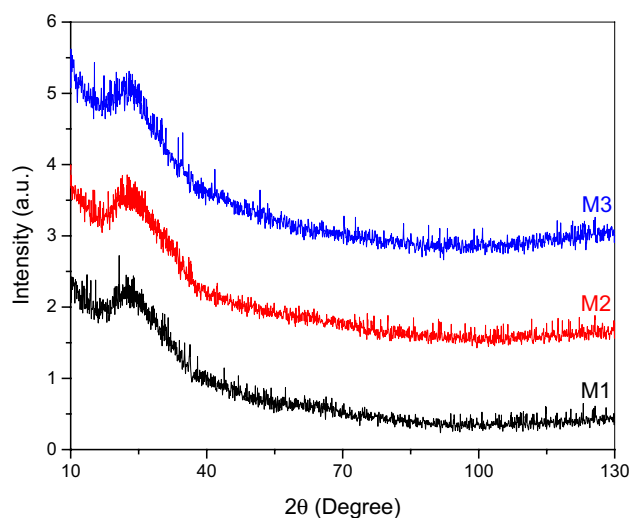


Fig. 4 XRD of BCP thin films prepared from solutions of different molarities

related to the melting process that resulted from a complete molecule unfreezing [19]. The last event located at 925 °C may be related to the breakdown of the molecular structure and then the decomposition of the BCP molecule.

Figure 3 also represents the TGA result curve which shows five thermal decomposition steps. The first step took place in 225–280 °C interval with about 25.7% weight loss followed by the 2nd step happened in 280–371 °C with an additional 16.8% weight loss. After that, the weight loss takes a slow rate behavior from 371 to 598 °C with additional weight loss of 9.7% followed by small decomposition step from 598 to 734 °C with 6.2% weight loss and then reached the final step of decomposition at 734 °C to the end of measurement temperature where the curve exhibits a very slow loss rate with 3.8% additional weight loss. The total weight loss is 62.2% in the temperature range 40–990 °C which indicates the good thermal stability of the BCP compound.

3.2 Structural and morphological analysis

Different molarities BCP thin films structural form appeared from X-ray diffraction approach (XRD) are sketched in Fig. 4. The resulted spectra of BCP thin films demonstrate a broad hump accompanied by a weak peaks suggesting the nanocrystalline nature of the prepared BCP thin films. An array of weak peak intensities of different heights that observed in the resulted diffractograms defining a polycrystalline shape of the prepared BCP organic material thin film. It's also noted that the molarity change did not strongly affect the crystalline structure of the resulted thin films prepared by spin coating.

The prepared BCP thin films morphology of BCP were inspected by scanning-electron-microscope (SEM) and high transmission electron microscope (HRTEM) as shown in Fig. 5. SEM resulted images of all molarities shows very fine particles with a good homogeneous distribution cover the whole substrate surface. The originated morphology is equivalent for all thin films of different molarities as represented in Fig. 5a–c respectively. This matching in morphology supports the evidence resulted from XRD analysis. By applying high transmission electron microscope to the thin film of molarity 3M, the image in Fig. 5d appears. It displays a tiny round (or spherical-like) grains (white background) allocated in a homogeneous manner all over the substrate surface. Many of these grains are agglomerated with each other forming the larger spherical black grains. A nearly 66 nm mean grain size was detected.

3.3 Optical absorption analysis

In spectral wavelength extent of (200–2500 nm), the films optical absorption spectra were captured through employing UV-visible spectrophotometer. The change of absorption coefficient upon incident photon energy investigation is carried out in the elevated absorption zones to understanding the band gaps details of the prepared films [23, 24]. The transmittance and reflectance change with the wavelength of BCP thin films of different molarities are shown in Fig. 6. It can be noticed that the reflectance is nearly constant with very low values while the transmittance changes strongly as the wavelength raises and reaches the saturation state at about 630 nm wavelength.

The spectrum reveals significant transmittance in the visible and infrared zones. Additionally, it is found that sharp fundamental absorption edge in the visible area at 630 nm wavelength. The transmittance and reflectance show nearly no distinct change with the molarity change.

Figure 7 displays the absorbance versus the wavelength for the prepared thin films of different molarities. The absorbance shows two peaks and one shoulder (or peak for the 2M film) at 285, 432, and 545 nm wavelength, respectively. These peaks are corresponding to different π - π^* transitions of the BCP molecule [13]. The shoulder on the high-wavelength side of samples M1 and M3 may be due to Jahn–Teller distortion of the excited states [25]. Jahn–Teller (JT) distortions occur when a non-linear molecule is in a degenerate electronic state. The molecule then distorts, its symmetry is lowered and the energy minimized [26]. It is observed that the absorbance increases with the increase of the molarity.

The absorption coefficient is predicted out of the absorbance employing the relation [27–29]:

$$\alpha = \frac{2.303A}{t} \quad (1)$$

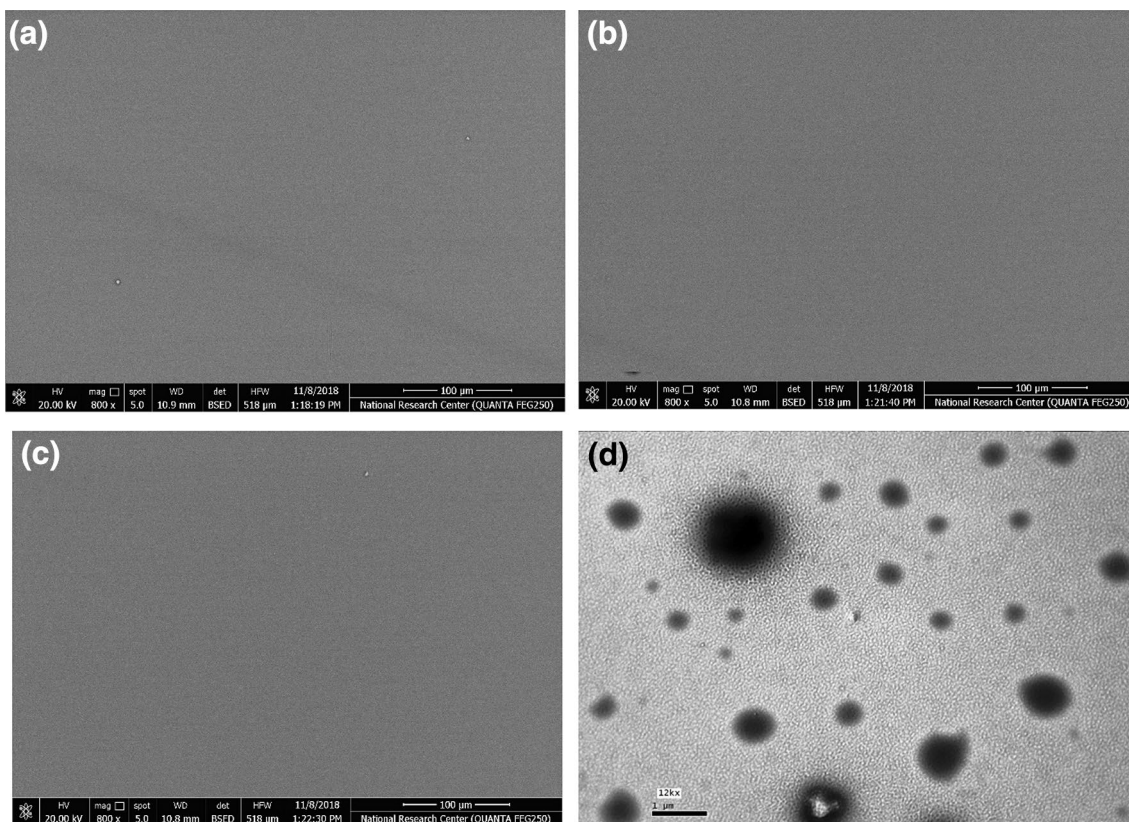


Fig. 5 Images of BCP thin films prepared from solutions of different molarities: SEM a 1M, b 2M, c 3M, and HTEM (d)

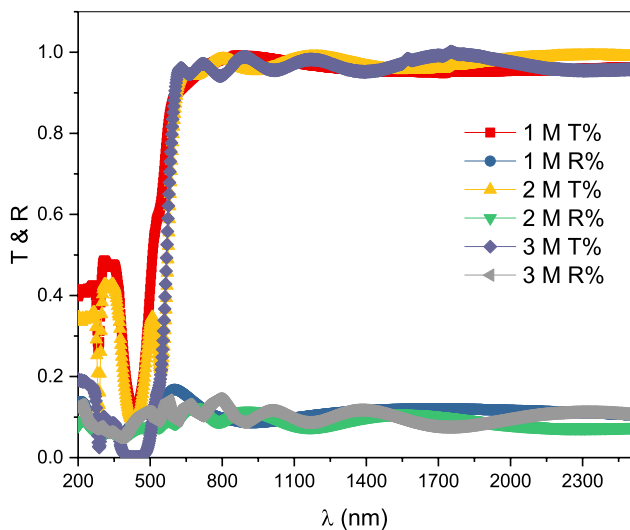


Fig. 6 The transmittance and reflectance change with the wavelength of BCP thin films of different molarities

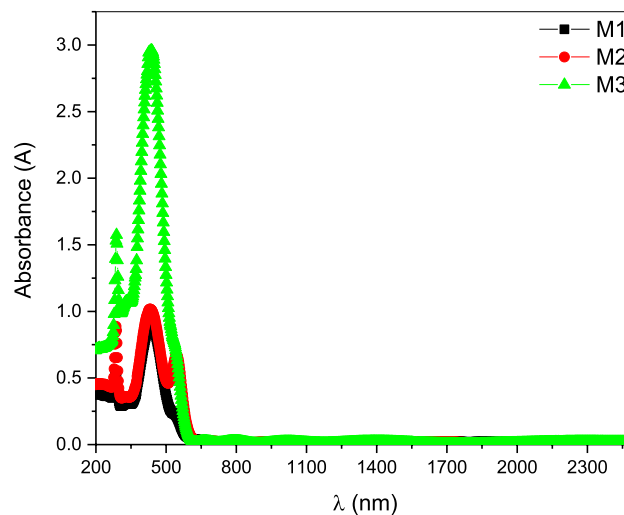


Fig. 7 the absorbance versus the wavelength for the prepared thin films of different molarities

where the absorbance, thickness, and absorption coefficient are represented by A , t , and α , respectively.

It was noted that all samples have a remarkable absorption coefficient in the range of 200–640 nm spectrum as viewed in Fig. 7 that monitors the absorption coefficient (α)

as a function of wavelength (λ) of BCP thin films of different molarities. The absorption coefficient goes up with the rise of the energy of the incident photon. The absorption coefficient has a value over 10^4 cm^{-1} which suggests that the

existence of direct transitions is higher. It was also detected that the absorption coefficient rises by molarity raising.

The optical energy gap (E_g) could possibly be estimated by employing two procedures. the first procedure is using Tauc function where the bandgap (E_g) is calculated by [30–32]:

$$\alpha h\nu = B(h\nu - E_g)^b \quad (2)$$

$$\ln(\alpha h\nu) = \ln B + b \ln(h\nu - E_g) \quad (3)$$

where α represents the absorption coefficient, $h\nu$ represents the falling photon energy, E_g represents the optical band gap, B represents a constant that is independent on falling photon energy and finally an exponent b that has 4 numerical values, $1/2$, 2 , 3 , and $3/2$ for allowed direct, allowed indirect, forbidden direct and forbidden indirect transitions, respectively.

To check the type of electronic transition if it is direct or indirect, the acquired relation between $\alpha h\nu$ and the photon energy $h\nu$, Fig. 8a, is fitted with Eq. (2) in the nearly linear end of the curve. The acquired variables were then inserted in Eq. (3) and sketched in Fig. 8b. As noticed, the optical transition type of all the prepared samples is direct with a power factor (the slope of linear relation) $b \approx 2$. As seen in Fig. 8c, direct bandgap was estimated by the extrapolation of a straight line of the curve linear portion to $(\alpha h\nu)^2 = 0$. It is noticed that the bandgap value is nearly the same (≈ 2.35 eV) for the three molarities thin films.

The second approach for estimating the optical energy gap is by analyzing the relation between the first derivative of absorbance with the energy of incident photon [33]. By capturing the absorbance 1st derivative as a function of incident photon energy, the optical energy gap will be the energy relates to the highest peak of the resulted curve as shown in Fig. 9. The shoulders on the low-energy side of *M1* and *M3* may be due to Jahn–Teller distortion of the excited states [25, 26]. It was found that the bandgap energy is the same for all molarities and equal to 2.81 eV. These results are in agreement with that estimated via Tauc function.

Urbach energy (E_u), the width of the localized states existing in the optical bandgap of the films, influences the optical gap arrangement and optical transitions. It is associated with the exponential tail of the density of states of both the two edges of the bandgap. The Urbach energy (E_u) is driven by [34]:

$$\alpha = \alpha_0 e^{h\nu/E_u} \quad (4)$$

where $h\nu$, α_0 , and E_u are the photon energy, constant, and Urbach energy respectively. Figure 10 illustrates the $(\ln\alpha)$ change with incident photon energy change for the prepared films of different molarities. E_u values were estimated as the reciprocal of slopes of the straight section of the relation

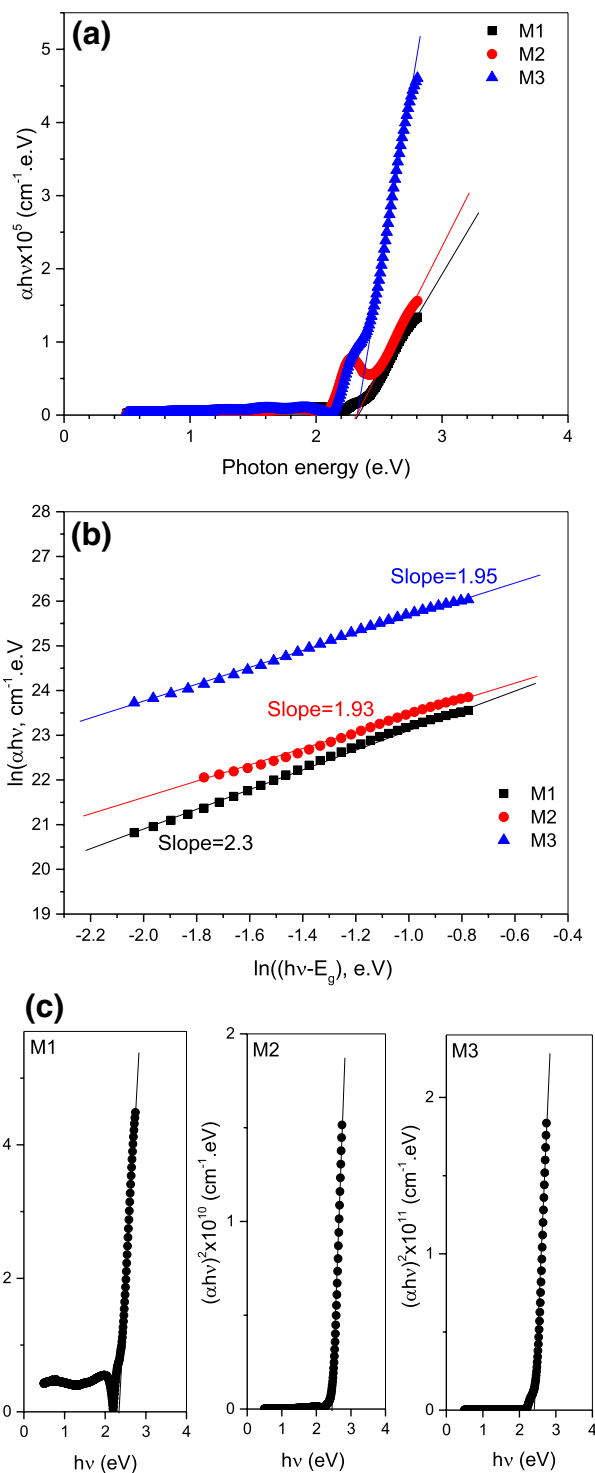


Fig. 8 $\alpha h\nu$ versus the photon energy $h\nu$ (a), $\ln(\alpha h\nu)$ versus $h\nu - E_g$ (b), and direct bandgap according to Tauc function

between $(\ln\alpha)$ and incident photon energy and was listed in Table 1. The Urbach energy is reduced by molarity rise.

The refractive index (n_r) is estimated employing the function [35]:

Fig. 9 The absorbance 1st derivative as a function of incident photon energy for thin films of different molarities

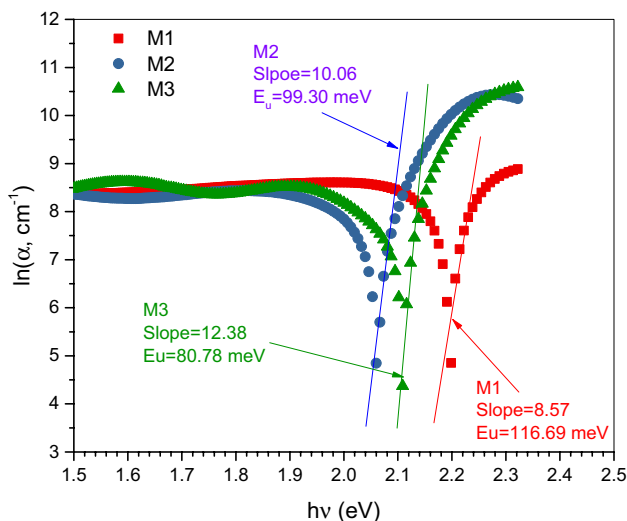
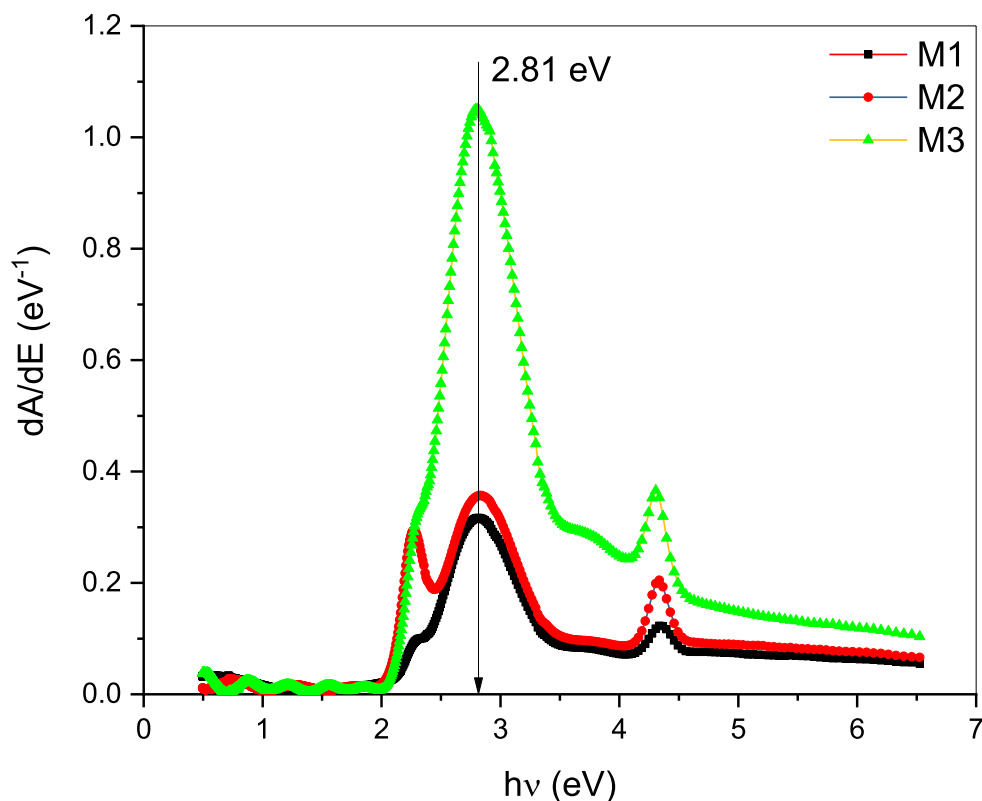


Fig. 10 The $\ln(\alpha)$ change with incident photon energy change for the prepared films of different molarities

Table 1 The resulted numerical values of E_d , E_0 , and the zero-photon energy refractive index, n_0 , for the prepared films with different molarities

| Molarity | E_d (eV) | E_0 (eV) | n_0 |
|----------|------------|------------|-------|
| M1 | 12.16 | 8.39 | 1.57 |
| M2 | 12.43 | 8.84 | 1.55 |
| M3 | 10.14 | 7.71 | 1.52 |

$$n_r = \left(\frac{(1 + R)^2}{(1 - R)^2} - (k_0^2 - 1) \right)^{\frac{1}{2}} + \frac{1 + R}{1 - R} \tag{5}$$

where n_r , R , and K_o are the refractive index, the reflectance, and the extinction coefficient respectively. The refractive index against wavelength for BCP thin films of different molarities is presented in Fig. 11. The evaluation outcomes reveal that the manufactured films refractive index n values are in the range of (1.4–2.45). The data shows a normal dispersion to which a single oscillator model can be applied. In that model [36], n is linked to the dispersion parameters (E_o and E_d) by [36]:

$$n_r^2 - 1 = E_o E_d / (E_o^2 - E^2) \tag{6}$$

where E , E_o , and E_d are the photon energy, the single oscillator energy, and the dispersion energy. E_o and E_d are directly calculated by the slope $(E_o E_d)^{-1}$ and the intersection (E_o/E_d) with the y axis. A plot of $1/(n^2 - 1)$ against $(hv)^2$ of BCP films of different molarities is displayed in Fig. 12. The resulted numerical values of E_o , E_d , and the zero-photon energy refractive index, n_0 , are recorded in Table 1.

The dielectric constant is symbolized as in the next form [30]:

$$\epsilon = \epsilon_1 - i\epsilon_2 \tag{7}$$

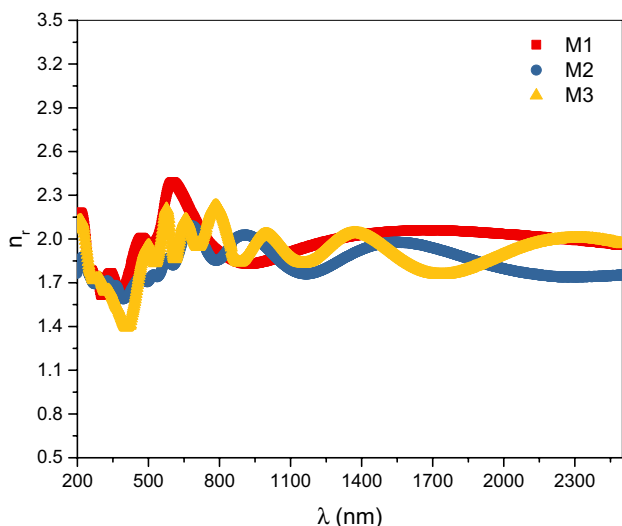


Fig. 11 The refractive index against wavelength for BCP thin films of different molarities

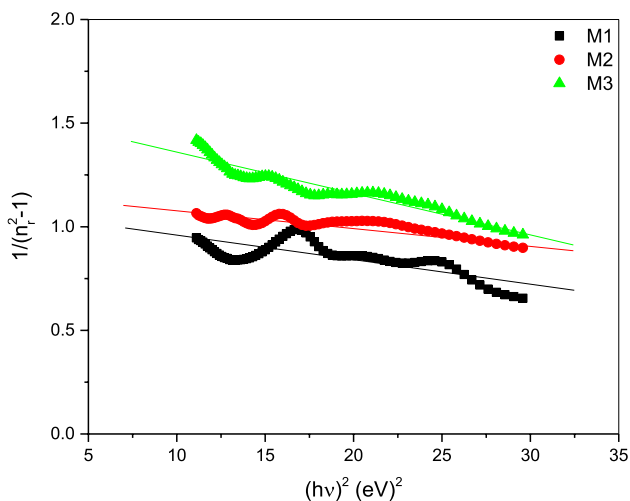


Fig. 12 A plot of $1/(n^2 - 1)$ against $(h\nu)^2$ of BCP films of different molarities

where ϵ_1 and ϵ_2 are the real part and the imaginary part of the complex dielectric constant. For the calculation of the two parts of a dielectric constant, the complex constant is resolved into its two parts as in next forms [34]:

$$\epsilon_1 = n^2 - k_o^2 \tag{8}$$

$$\epsilon_2 = 2nk_o \tag{9}$$

The change of real and imaginary components of dielectric constant with the change of incident photon energy for BCP thin films with different molarities is represented in Fig. 13. The two components, real and imaginary, of the dielectric constant, are nearly unchanged as incident

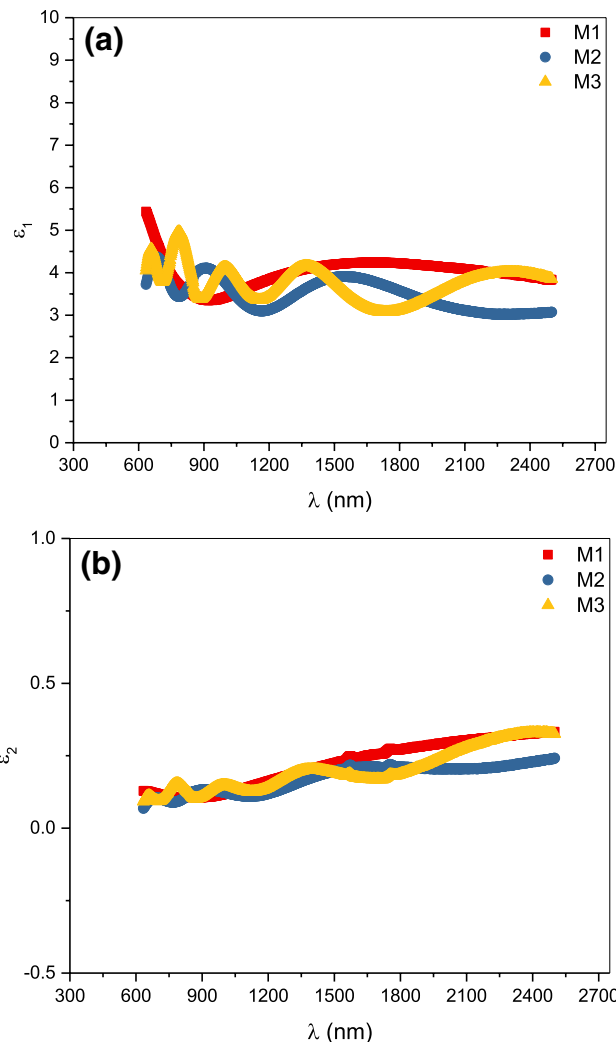


Fig. 13 The change of **a** real and **b** imaginary components of dielectric constant with the change of incident photon energy for BCP thin films with different molarities

photon wavelength change from 600 to 2500 nm. In addition, the values of the real and imaginary components nearly unchanged with molarity change.

3.4 I–V characteristics in dark conditions

The prepared Au/BCP/p-Si/Al diode current and voltage (I – V) features that assessed at steady temperatures are drawn in Fig. 14. The remarkably excessive values of current in the forward direction than that of the reverse direction authorize the junction rectifying. The relationship running between the diode natural logarithm of forward-current and the working potential at fixed temperatures is sketched in Fig. 15. At definitely low working potentials ($V \leq 1.06$ volts) the relationship behavior is linear and changed to curvy behavior at higher potentials ($1.06 < V \leq 2$). This response definitely

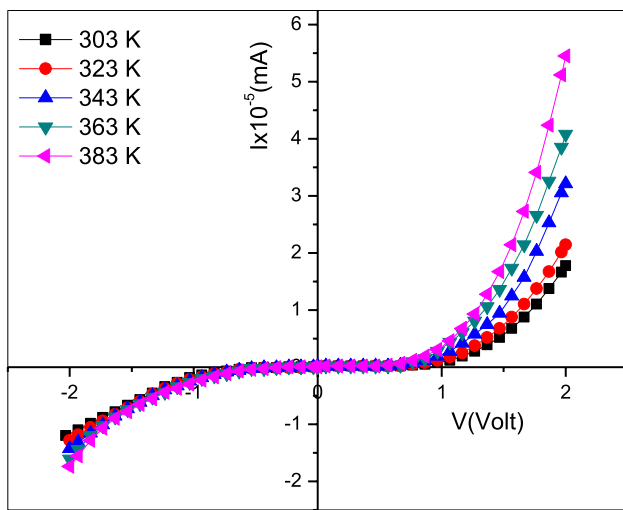


Fig. 14 The I–V characteristics of Au/BCP/p-Si/Al heterojunction diode measured at fixed temperatures

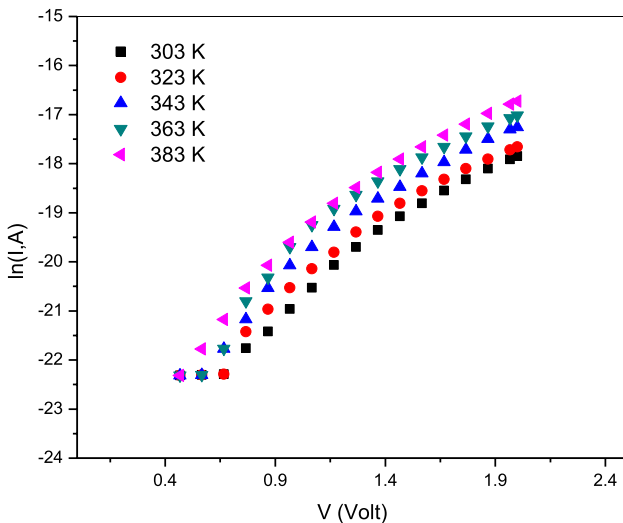


Fig. 15 The variation of the $\ln(I)$ with V for Au/BCP/p-Si/Al diode at settled temperatures

is generated from the series resistance (R_s) that frequently performed by the resistance of electrical cabling, deposited BCP layer, n-Si chip.

Table 2 The values of n and ϕ_B as a function of temperature calculated from (I – V) measurements and Nord function

| T (K) | I – V | | F (V) | | | |
|---------|-----------|---------------|------------------------|------------------|------------------------|------------------|
| | n | ϕ_B (eV) | R_{s1} (K Ω) | ϕ_{B1} (eV) | R_{s2} (K Ω) | ϕ_{B2} (eV) |
| 303 | 11.1 | 1.04 | 138.6 | 0.79 | 51.8 | 0.92 |
| 323 | 8.8 | 1.11 | 134.2 | 0.85 | 27.39 | 0.99 |
| 343 | 7.1 | 1.19 | 123.4 | 0.91 | 21.94 | 1.05 |
| 363 | 5.9 | 1.28 | 23.4 | 0.97 | 8.5 | 1.16 |
| 383 | 5.2 | 1.33 | 21.3 | 1.02 | 3.7 | 1.19 |

Within a low-forward potential region, the current transport through the prepared BCP/p-Si contact is discussed with the approach of standard diode [21]:

$$I/I_0 = e^{(qV/nkT)} - 1 \tag{10}$$

where I_0 , q , V , n , k , T signifies the reverse saturation current, the electron charge, the applied potential, the contact ideality factor, the Boltzmann’s constant, and the absolute temperature, respectively.

The reverse saturation current (I_0) is provided by [20]:

$$I_o = AA^* T^2 \exp (q\phi_B/KT) \tag{11}$$

Here, A , A^* , ϕ_B signifies the contact effective area, the Richardson constant ($32 \text{ A cm}^{-2} \text{ K}^{-2}$) for p-Si [22], and the effective barrier height at 0 bias.

Through the use of the straight portion of the resulted relationship among the current natural logarithm ($\ln I$) and the loaded potential (V) in the forward direction, the prepared junction barrier height (ϕ_B) and ideality factor (n) are calculated and included in Table 2. The ideality factor (n) drop and the barrier height (ϕ_B) improvement by heating are noted from the tabulated data and it is originated from the inhomogeneity of the contact barrier height [20, 37]. Throughout the lower temperature conditions, carriers charges (i.e. electrons) are qualified to beat the weak barriers and the current moves across it [30, 38], but with the temperature boost, extra charge carriers will collect additional energy to overcome the larger barriers [19, 35]. Hence, with the applied potential and heating boost, the barrier height turns into more significant values. The contact delivers an ideal factor above unity and this is often growing by the interfacial states, series resistance, tunneling, and inhomogeneous barrier height [37].

The series resistance, R_s , is actually an important variable for the junction particularly when the voltage impacts the I – V features of a junction. The values of deposited BCP/p-Si contact series resistance (R_s) is detected simply by the revised Norde’s formula assistance [19]:

$$F(V) = \frac{V}{X} - \frac{kT}{e} \ln \left(\frac{I(V)}{AA^*T^2} \right) \tag{12}$$

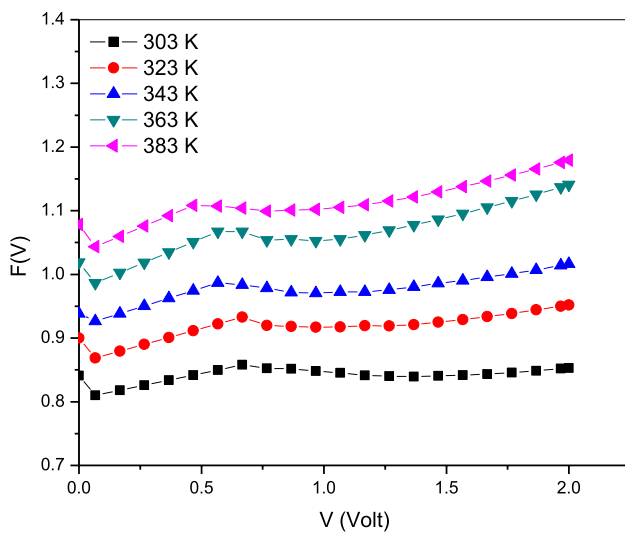


Fig. 16 Nord's function of Au/BCP/p-Si/Al diode

where X represents the 1st integer over the ideality factor value. $I(V)$ represent the current. The R_s value at different heating temperatures is predicted via the next formula [25]:

$$R_s = \left(\frac{kT}{e} \right) \left(\frac{X - m}{I(V_o)} \right) \quad (13)$$

where $I(V_o)$ signifies the current corresponding to the voltage lowest point of $F(V)$ versus V curve.

The barrier height is computed with [39]:

$$\phi = F(V_o) + \frac{V_o}{X} - \frac{kT}{e} \quad (14)$$

where $F(V_o)$ and V_o signifies the $F(V)$ corresponding to the voltage lowest point of $F(V)$ versus V curve and the corresponding voltage value.

Two distinctive minima were realized in the Norde function curves as noticed in Fig. 16. Therefore, two different values of the barrier height and also the series resistance were delivered (named ϕ_{b1} , R_{s1} , and ϕ_{b2} , R_{s2}). This behavior was reported by Parish et al. [40] for n-GaN Schottky diodes and it was interpreted as two diodes in parallel and attributed to the presence of screw dislocations [41].

Considering Fig. 16 of Norde's equation along with Eqs. 12 and 13, the values of both the barrier height and the series resistance of the prepared junction at different temperatures are got and are placed in Table 2. The decrease of both R_{s1} and R_{s2} and the boost of the ϕ_{b1} and ϕ_{b2} with heating is observed from the tabulated data in Table 2. The ϕ_{b1} was in approximately matching to the barrier height extracted from I–V results, whilst the other, ϕ_{b2} , was much higher and with much lower series resistance. The differences between the

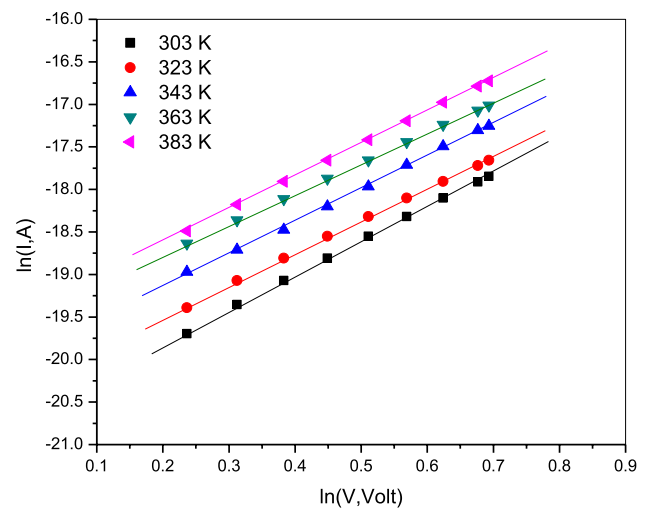


Fig. 17 $\ln I$ – $\ln V$ characteristic of higher forward applied voltages region

values of barrier height got from Norde's calculations and that received via I–V data are influenced by the dissimilarity of calculation procedures [42].

The impact of larger employed voltages in the forward direction to the contact I–V aspects are evaluated by graphing $\ln I$ with $\ln V$ as provided in Fig. 17. The outcome layout exhibits a straight-line response of a slope ≈ 4 . That conclusion ensures that the conduction mechanism in the present case is the space charge limited current dominated by the exponential trap of distribution [41]. So, that result shows that the BCP layer conduction procedure supplies an effect to the synthesized junction I–V properties [29, 43].

4 Conclusions

Thin films of organic compound BCP were successfully prepared by a simple spin-coating approach from solutions of different molarities. DSC and TGA of the starting powder prove the thermal stability of the compound to about 225 °C. The produced different molarities thin films structural and morphological evaluation displayed their nanostructure arranging form. HRTEM images identify the films particle sizes of about 66 nm. The optical evaluation revealed nearly no change of energy gap, refractive index, real and imaginary dielectric constant with change in molarity. The Dark I–V specifications of Al/p-Si/BCP/Au fabricated device at different temperature was investigated. It was found that the increase of temperature leads to the decrease of ideality factor, an increase of barrier height, and a decrease of series resistance, respectively.

References

1. A.A.M. Farag, W.G.G. Osiris, A.H.H. Ammar, A.M. Mansour, *Synth. Met.* **175**, 81 (2013)
2. R. Farchioni, G. Grosso, *Organic Electronic Materials* (Springer, Berlin, 2001)
3. M. Knaapila, *Conjugated Polymers and Oligomers: Structural and Soft Matter Aspects* (World Scientific Publishing Co Pte Ltd, Singapore, 2017)
4. D. C. Siegmund Roth, in *One-Dimensional Metals: Conjugated Polymers, Organic Crystals, Carbon Nanotubes*, 2nd edn. (Wiley, Weinheim, 2004)
5. M.R. Grimmett, in *Sci* (Synth, Houben-Weyl Methods Mol Transform (Thieme, Stuttgart, 2002)
6. J.R. Sheats, *J. Mater. Res.* **19**, 1974 (2004)
7. W. Brütting, *Physics of Organic Semiconductors - Preface* (Wiley, Weinheim, 2004)
8. C.R. Newman, C.D. Frisbie, DA da Silva Filho, JL Brédas, PC Ewbank, KR Mann. *Chem. Mater.* **16**, 4436 (2004)
9. F.M. Schabel, H.E. Skipper, L. White, W.R. Laster, *Cancer Res.* **21**, 700 (1961)
10. Z. Dechun, *Org Light Diodes Mater Devices Appl* (Woodhead Publishing, Sawston, 2013), pp. 114–142
11. J.D. Myers, J. Xue, *Polym. Rev.* **52**, 1 (2012)
12. A.Y. Al-Ahmad, M.F. Al-Mudhaffer, H.A. Badran, C.A. Emshary, *Opt. Laser Technol.* **54**, 72 (2013)
13. S. Koçak, B. Aslışen, *Sensors Actuators. B Chem.* **196**, 610 (2014)
14. P.C. Ray, P.K. Das, *J. Phys. Chem.* **99**, 14414 (1995)
15. C.A. Walsh, D.M. Burland, V.Y. Lee, R.D. Miller, B.A. Smith, R.J. Twieg, W. Volksen, *Macromolecules* **26**, 3720 (1993)
16. Y. Wang, L.L. Tong, *Sensors Actuators. B Chem.* **150**, 43 (2010)
17. S. Choudhury, R. Chitra, J.V. Yakhmi, *Thin Solid Films* **440**, 240 (2003)
18. S. Shrestha, R.J. Mascarenhas, O.J. D'Souza, A.K. Satpati, Z. Mekhalif, A. Dhason, P. Martis, *J. Electroanal. Chem.* **778**, 32 (2016)
19. A.M. Mansour, *Silicon*, 1 (2018) (in press)
20. A.A.M. Farag, F.S. Terra, G.M. Mahmoud, A.M. Mansour, *J. Alloys Compd.* **481**, 427 (2009)
21. F.S. Terra, A.A. Higazy, G.M. Mahmoud, A.M. Mansour, *Indian J. Phys.* **84**, 265 (2010)
22. E.M. El-Menyawy, A.M. Mansour, N.A. El-Ghamaz, S.A. El-Khodary, *Phys. B Condens. Matter* **413**, 31 (2013)
23. A.M. Mansour, F.M.A. Taweel, R.A.N. Abu El-Enein, E.M. El-Menyawy, *J. Electron. Mater.* **46**, 6957 (2017)
24. M. Husham, Z. Hassan, A.M. Selman, N.K. Allam, Sen. *Actuators A Phys.* **230**, 9 (2015)
25. D. Gui, L. Ji, A. Muhammad, W. Li, W. Cai, Y. Li, X. Li, X. Wu, P. Lu, *J. Phys. Chem. Lett.* **9**, 751 (2018)
26. R. Freitag, J. Conradie, *J. Chem. Educ.* **90**, 1692 (2013)
27. A.M. El Nahrawy, A.M. Mansour, A.B. Abou Hammad, A.R. Wassel, *Mater. Res. Express* **6**, 016404 (2019)
28. A.A. Azab, E.M. El-Menyawy, A.M. Mansour, G.M. Mahmoud, F.S. Terra, *Recent Patents. Mater. Sci.* **11**, 41 (2018)
29. A.A.M. Farag, A.M. Mansour, A.H. Ammar, M.A. Rafea, A.M. Farid, *J. Alloys Compd.* **513**, 404 (2012)
30. A.A.M. Farag, A.M. Mansour, A.H.H. Ammar, M.A.A. Rafea, *Synth. Met.* **161**, 2135 (2011)
31. I.M. El Radaf, M. Nasr, A.M. Mansour, *Mater. Res. Express* **5**, 015904 (2018)
32. N. Hassan, A.M.M. Mansour, N. Roushdy, A.A.M.A.M. Farag, W.G.G. Osiris, *Optik (Stuttg.)* **158**, 1255 (2018)
33. A.A.M. Farag, H.S. Soliman, A.A. Atta, *Synth. Met.* **161**, 2759 (2012)
34. A.M. Mansour, A.A.M. Farag, *Organo Opto Electr. An Int. J.* **35**, 29 (2016)
35. A.M. Mansour, I.S. Yahia, I.M.E. Radaf, *Mater. Res. Express* **5**, 076406 (2018)
36. A.M. El Nahrawy, A.B.A. Hammad, A.M. Youssef, A.M. Mansour, A.M. Othman, *Appl. Phys. A Mater. Sci. Process.* **125**, 46 (2019)
37. I.M. El Radaf, A.M. Mansour, G.B. Sakr, *J. Semicond.* **39**, 124010 (2018)
38. M. Nasr, A. M. Mansour, and I. M. El Radaf, *Mater. Res. Express* **6**, (2019).
39. A.A.M. Farag, F.S. Terra, G.M.M. Fahim, A.M. Mansour, *Met. Mater. Int.* **18**, 509 (2012)
40. G. Parish, R.A. Kennedy, G.A. Umana-Membreno, B.D. Nener, *Solid. State. Electron.* **52**, 171 (2008)
41. Y. Huang, X.D. Chen, S. Fung, C.D. Beling, C.C. Ling, *J. Appl. Phys.* **94**, 5771 (2003)
42. A.A.M. Farag, F.S. Terra, A. Ashery, G.M.M. Fahim, A.M. Mansour, *Indian J. Pure Appl. Phys.* **56**, 203 (2018)
43. A.A.M. Farag, F.S. Terra, A. Ashery, A.M. Mansour, *Optoelectron. Adv. Mater. Rapid Commun.* **11**, 82 (2017)

Publisher's Note Springer Nature remains neutral with regard to jurisdictional claims in published maps and institutional affiliations.